Bidirectional AC–DC Modular Multilevel Converter With Electric Spring Functions for Stabilizing Renewable AC Power Grid at the Distribution Voltage Level

Hin Sang Lam, *Graduate Student Member, IEEE*, Huawei Yuan, *Member, IEEE*, Siew-Chong Tan, *Senior Member, IEEE*, Chunting Chris Mi, *Fellow, IEEE*, Josep Pou, *Fellow, IEEE*, and S. Y. R. Hui, *Fellow, IEEE*

***Abstract*— Bidirectional ac–dc power converters are essential in emerging smart grids with increasing renewable energy penetration. This article presents a bidirectional ac–dc power converter system comprising modular multilevel converters (MMCs) and dual active bridges (DABs) with medium-frequency transformer isolation designed for linking an ac distribution voltage of 6.6 kV to a dc grid of 800 V for future electric vehicle (EV) charging infrastructure. The novel contributions include: 1) a modular method to power EV charging infrastructures in multistorey carparks without mains-frequency transformers and 2) the incorporation of a front-end control with electric spring (ES) functions that enable the dc power grid with battery energy storage to interact dynamically with the ac power grid at the distribution voltage level to achieve instantaneous power balance and hence system stability. The long-term aim is to use large EV charging infrastructures to stabilize increasing intermittent renewable energy via the proposed ac–dc converter, consequently accelerating the adoption of large-scale renewable energy and EV as a complementary solution to combat climate change. This article focuses on the bidirectional ac–dc converter of this overall idea based on the MMC and DAB technologies as an example. Results on the power converter operation level and ac microgrid level are included.**

***Index Terms*— Demand-side management (DSM), electric springs (ESs), power system stability, smart grids.**

Manuscript received 11 January 2022; revised 11 March 2022 and 17 April 2022; accepted 1 May 2022. Date of publication 9 May 2022; date of current version 6 December 2022. This work was supported in part by the Nanyang Technological University (NTU) MediaTek Endowment Fund under Grant 03INS001124C140 and in part by the NTU Research Exploration under Grant 03INS001253C140. Recommended for publication by Associate Editor Grain Philip Adam. *(Corresponding author: S. Y. R. Hui.)*

Hin Sang Lam, Huawei Yuan, and Josep Pou are with the School of Electrical and Electronic Engineering, Nanyang Technological University, Singapore 639798 (e-mail: hinsang001@e.ntu.edu.sg; huawei.yuan@ntu.edu.sg; josep.pou@ieee.org).

Siew-Chong Tan is with the Department of Electrical and Electronic Engineering, University of Hong Kong, Hong Kong (e-mail: sctan@eee.hku.hk).

Chunting Chris Mi is with the Department of Electrical and Computer Engineering, San Diego State University, San Diego, CA 92182 USA (e-mail: cmi@sdsu.edu).

S. Y. R. Hui is with the School of Electrical and Electronic Engineering, Nanyang Technological University, Singapore 639798, and also with the Department of Electrical and Electronic Engineering, Imperial College London, London SW7 2BX, U.K. (e-mail: ron.hui@ntu.edu.sg).

Color versions of one or more figures in this article are available at https://doi.org/10.1109/JESTPE.2022.3173809.

Digital Object Identifier 10.1109/JESTPE.2022.3173809

I. Introduction

POWER electronics converters are increasingly being connected to ac power systems with increasing renewable energy penetration. The Paris Agreement under the framework of the United Nation on Climate Change [1] has prompted many governments to set targets to drastically reduce greenhouse gas emission. In March 2021, the Singapore Government announced the 2030 Green Plan [2], which contains major initiatives of increasing renewable energy generation and replacing combustion vehicles with electric vehicles (EVs).

Two technical hurdles must be overcome to realize these Green Plan initiatives. First, replacing combustion vehicles with EV is only meaningful if the EVs are charged by renewable energy. Charging the EVs with fossil-fuel electricity generation defeats the Green Plan purpose. Means to equip many existing multistorey carpark buildings with electric power infrastructure for EV charging is urgently needed. Second, solar energy is preferred because the wind energy resource is limited in Singapore. However, solar power generation is highly weather-dependent and intermittent in nature. It has been reported [3] that the rate of solar power change of a 1000 m^2 photovoltaic (PV) array can be as high as 5 MW/s for cloud moving at 20 m/s. For faster cloud movement, such power variation rate can be doubled to 10 MW/s. For power system stability, it is essential to maintain instantaneous balance between power supply and load demand [4]. With the increasing use of intermittent renewable energy resources, there is a need to change the control paradigm from "power supply following load demand" to "load demand following power supply" [5], [6].

Several methods can be considered for meeting the power balance requirement. They can be broadly classified as supply-side management (SSM), demand-side management (DSM), and energy storage. SSM refers to actions taken to ensure that the generation, transmission, and distribution of energy are conducted efficiently. In the past, the control of power generation was primarily carried via the control of the generators, which have relatively large inertia and thus time constant.

Recently, fast control of renewable energy sources has become an emerging research area. Although maximum power point tracking of PV panels and wind turbines (WTs) has been well conceived, curtailing renewable energy generation has gained more attention [7], as the prices of renewable energy sources such as PV panels continue to drop. Similar SSM argument can be considered for curtailment of wind power [8].

DSM has been adopted by power companies to reduce peak power. Examples of traditional DSM are scheduling of delay-tolerant power demand tasks [9], [10], real-time pricing [11], [12], and direct load control or ON–OFF control of smart loads [13], [14]. However, these traditional methods have relatively long response timescales (i.e., tens of minutes to days ahead) and cannot deal with instantaneous power balance of supply and demand. Therefore, the emerging power grids require a new control paradigm and advanced technologies, such as power electronic facilities and energy storage systems. In recent years, power-electronics-based technology such as electric spring (ES) technology with response time of milliseconds [15], [16] has been proposed as the fast and real-time DSM solutions. ESs have been associated with noncritical loads such as thermal loads to form smart loads that can consume power adaptively at the low-voltage ac mains level. If distributed widely over the low-voltage ac mains network, smart loads with ES technology can absorb power fluctuations arising from intermittent renewable power generation. Energy storage is an obvious solution to balance the differences between power supply and demand. Examples are batteries, flywheels [17], and water reservoirs. However, safety, costs, and geographical limitations are the considerations for energy storage.

The global push for EVs is expected to create a demand for large-scale EV charging facilities [18], [19]. Such infrastructures should be capable of charging hundreds of 1000 EVs and will require high-power installations in the multimegawatt range. Recent proposals of high-voltage-ratio dc–dc converters based on multilevel converters (MLCs) [20] and modular multilevel converters (MMCs) [21]–[23] open a door to power large EV charging infrastructures at the distribution level. This article illustrates the idea of using the MMC with ES functions at the power distribution systems to stabilize the ac power grid with the energy storage in the EV charging infrastructure. In Section II, the basic concept of the ES and possible topologies are briefly explained. Section III explains the controller design of the ES. Section IV provides the simulation results under different power system scenarios. Finally, this article is concluded in Section V.

II. Novelty of the Proposed Bidirectional Power Converters With Electric Spring Functions

The novel contributions of this article include: 1) a flexible and modular method with the potential to power EV charging infrastructures in multistorey carparks without mains-frequency transformers and 2) the use of the ES functions in the ac–dc power converter at the distribution voltage level to enable the dc power grid with battery energy storage to interact dynamically with the ac power grid at the distribution voltage level to achieve instantaneous power balance and hence system stability. The long-term aim is to use large EV charging infrastructures to stabilize increasing intermittent renewable energy via the proposed ac–dc converter, consequently accelerating the adoption of large-scale renewable energy and EV as a complementary solution to combat climate change.

In this article, a bidirectional ac–dc MMC with ES functions is proposed and investigated. There are four major differences between previous ES works and this project.

1) ESs were previously connected to the low-voltage ac mains voltage (i.e., typically 110 V for 60 Hz or 220–240 V for 50 Hz), while the new ES is connected to the medium-voltage distribution voltage network.
2) Previous ESs were primarily based on two-level inverter associated with noncritical loads, while this project involves a bidirectional ac–dc MMC/MLC with dual active bridges (DABs) for association with a 800-V dc power grid suitable for powering large EV charging infrastructure with both EV batteries and second-life batteries.
3) The modular feature of this MMC proposal enables the power supply capability to be flexibly expanded for the dc-grid-powered EV charging infrastructure according to the parking capacities in the multistorey carpark buildings without using mains-frequency transformers.
4) The control loops in the ES in this project involve both input voltage and frequency control of the ac distribution network and voltage regulation of the dc power grid.

Since the semiconductor switch can withstand a limited voltage rating, the previous two-level voltage source inverter for low-voltage ES is not suitable for the medium-voltage distribution system (typically at 6.6–22 kV). Therefore, two feasible circuit topologies will be introduced. Fig. 1 illustrates the core concept of the bidirectional MMC linking the ac distribution lines of a power system with a mixture of intermittent renewable and traditional energy sources. The distribution lines have a lot of nodes that contain different kinds of loads and renewable energy sources. One of the nodes is connected to the proposed ac–dc power converter that converts the ac distribution voltage to an 800-V dc link for a dc power grid. The dc power grid can be used for large EV charging infrastructure with EV batteries and preferably second-life batteries as energy storage.

The focus of this article is the use of the ES functions embedded on the ac side of the bidirectional MMC to turn the dc-grid-power EV charging infrastructure into a form of smart load that can consume energy from or deliver energy to the ac power system at the distribution level [24]. The purpose of this research is to provide a unit model that will be used in future studies with hundreds of such ES-based EV charging infrastructures in the multistorey carparks, which can help to support and stabilize the power grid in megacities (such as Singapore) with a large percentage of renewable energy penetration. While MMC circuits have previously been reported, the incorporation of ES functions [15], [16], [24] adds new control of active and reactive power compensation for mains-frequency and mains-voltage regulation for the ac

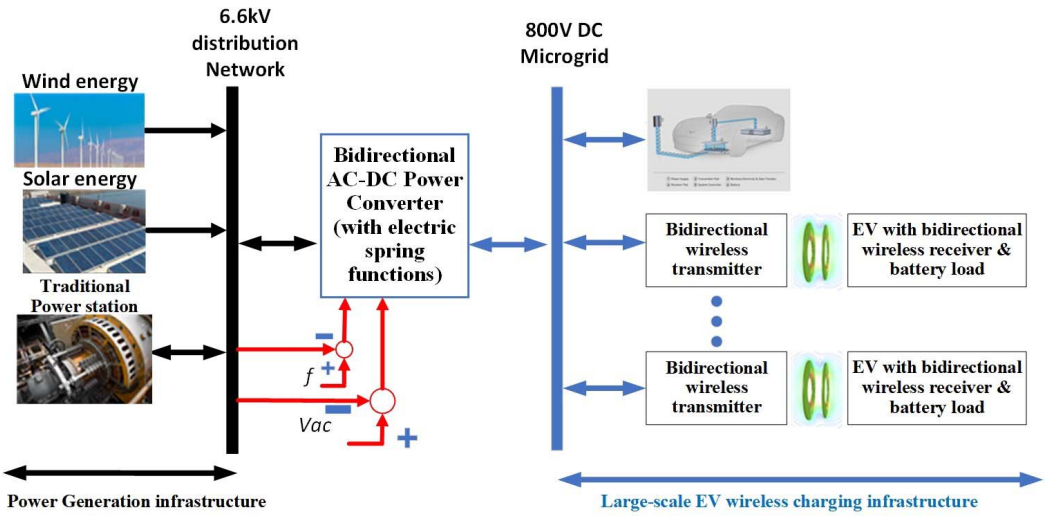

Fig. 1. Schematic of the proposed bidirectional ac power converter linking the ac distribution line of the ac power system to voltage link of the dc power grid.

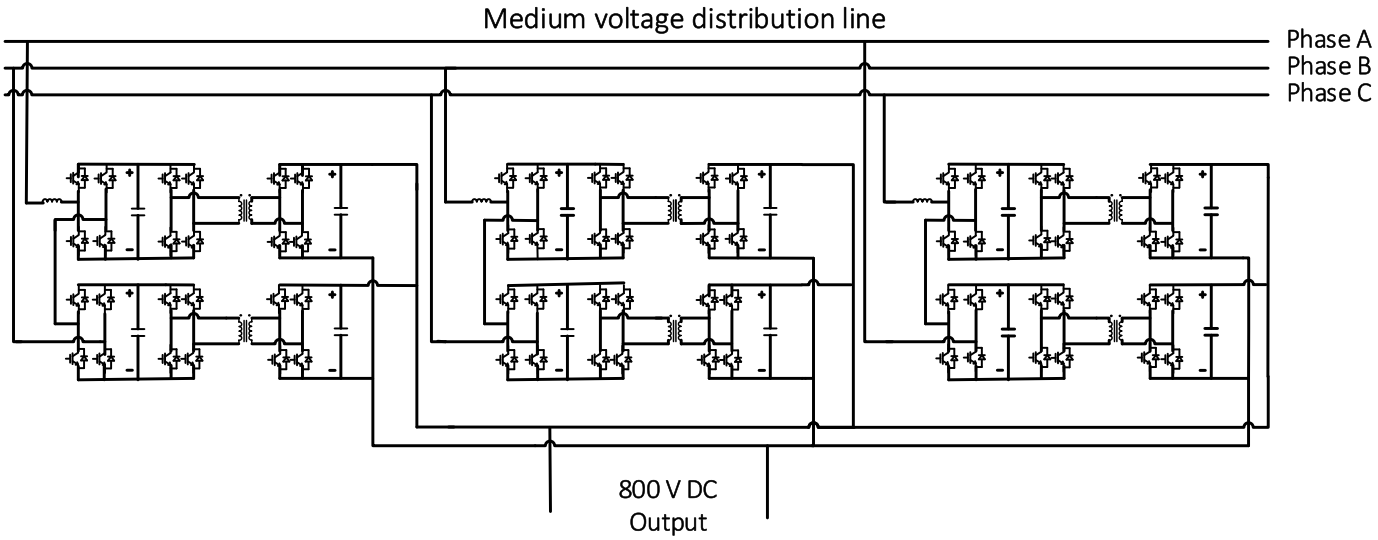

Fig. 2. Example of using an MMC as the front-end power converter for the proposed bidirectional power converter (evaluated in this study).

power system, respectively, at the distribution level. In this way, the large EV charging infrastructure with the bidirectional MMC neutralizes the problems arising from renewable energy generation. It forms the new ES system to stabilize the ac power system with intermittent renewable energy generation.

A. Modular Multilevel Converter (MMC)

One natural family of power electronic circuits suitable for the first ac–dc power conversion stage of the proposed idea is the MMC circuits [25]–[27]. Since the publication of [25], various research efforts have led to a family of MMC topologies [26], [27], including those with high-voltage ratios [20]–[23]. In this article, we suggest a new version of such implementation, which is shown in Fig. 2. In this example, the bidirectional converter consists of: 1) a front-stage ac–dc MMC; 2) an intermediate dc–ac power converter with a medium-frequency isolation transformer for voltage reduction; and 3) a third ac–dc power converter to create the voltage source for the dc power grid. DAB [28] can be used in the intermediate power stage. The loads in this system are assumed to be battery loads in EV charging infrastructure.

In each module of the MMC example in Fig. 2, an inductor and a full-bridge inverter with an output capacitor are used for power-factor-correction (PFC) front-end power conversion. The number of MMC modules is determined by the distribution line voltage and the voltage ratings of the power devices. Presently, Si-based insulated-gate bipolar transistors (IGBTs) are suitable for MMC implementation. In the future, SiC power devices will have the potential for MMC implementation due to their high-voltage ratings. In the intermediate dc–ac power conversion stage, a medium-frequency power inverter is used to turn the dc voltage into a medium-frequency ac voltage through a step-down isolation transformer. The step-down secondary ac voltage outputs of the isolation transformer

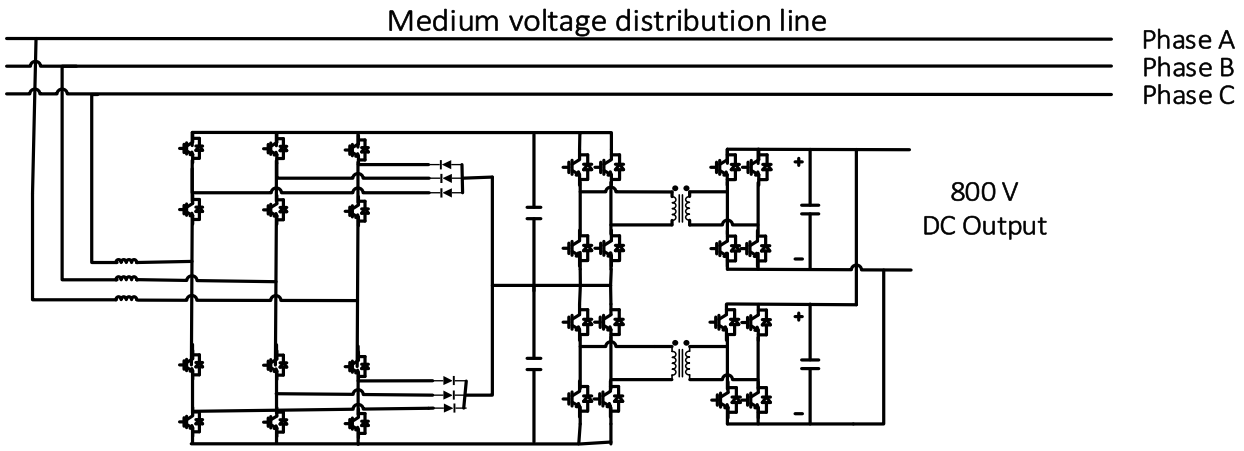

Fig. 3. Example of using an MLC (three-level neutral-point-clamed MLC) as the front-end power converter for the proposed bidirectional power converter (for future study).

are converted into a dc voltage in the final-stage ac–dc power converter. The three dc voltage outputs in Fig. 2 can be connected in parallel to form one dc voltage for the dc power grid.

B. Multilevel Converter (MLC)

An alternative family of power electronic circuits is the MLCs [29]. Like the circuit shown in Fig. 3, this bidirectional ac–dc power conversion system has three power stages. One example of using a three-level neutral-clamped power converter as the first ac–dc power converter in the proposed bidirectional ac–dc power conversion system is shown in Fig. 3. The dc voltages across the two dc capacitors are stepped down into medium-frequency ac voltages by the intermediate dc–ac power inverter with transformer isolation. The ac voltages from the secondary of the isolation transformers are then converted into a dc voltage in the third ac–dc power conversion stage to form the dc power grid. Again, the DAB topology can be used in the intermediate power stage.

III. Converter Operation and Power System Studies

Due to the limited space in this article, the MMC topology (see Fig. 2) is used as an example for demonstrating the proposed idea. The MLC topology (see Fig. 3) will be addressed in future work. This section presents the circuit composition, the controller design, and the average model of the proposed bidirectional ac–dc power conversion system and its interactions with a micro power grid in a stage-by-stage manner for the MMC system in Fig. 2. The purpose is to study the feasibility of the proposal on a relatively small scale before system evaluation in large-scale power systems. The 6.6-kV distribution line voltage in Singapore is taken as the first design study. Such a design can be extended to 11 or 22 kV in principle.

A. Bidirectional AC–DC Power Converter System With Front-End MMC With Electric Spring Functions

1) First AC–DC PFC Power Conversion: The ac–dc stage is a cascaded full-bridge rectifier, which supports bidirectional power flow as required for achieving ES functions. The number N_{HB} of the full-bridge modules is determined by the voltage level of the distribution network. According to [30], N_{HB} can be calculated by

$$N_{\mathrm{HB}} = \frac{\sqrt{2}\ V_g}{u V_{\mathrm{sw,max}}} \tag{1}$$

where V_g is the line-to-line rms voltage of the distribution network, $V_{\mathrm{sw,max}}$ is the maximum voltage that each semiconductor switch can bear, u is the utilization of $V_{\mathrm{sw,max}}$, and u is the utilization rate of the voltage rating of semiconductor switches and satisfies $u \leq 1$. For a 6.6-kV grid voltage (i.e., $V_g = 6.6$ kV), the value of $V_{\mathrm{sw,max}}$ is listed in Table I, in which $u = 55\%$ and $N_{\mathrm{HB}} = 1$–3 [30]. Table I indicates that three full-bridge modules are needed in the rectifier with 6500- V IGBTs or two modules are needed with the 10-kV silicon-carbide metal–oxide–semiconductor field-effect transistors (SiC MOSFETs) [31].

TABLE I
Required Voltage Ratings of Switches for a 6.6-kV Power Grid

V_{g}	6.6 kV
u	55%
$V_{\mathrm{sw,max}}$ when $N_{\mathrm{HB}} = 1$	16.9 kV
$V_{\mathrm{sw,max}}$ when $N_{\mathrm{HB}} = 2$	8.49 kV
$V_{\mathrm{sw,max}}$ when $N_{\mathrm{HB}} = 3$	5.7 kV

In our simulation study, the rectifier that consists of two full-bridge modules is used as an example to demonstrate the idea of this article, as shown in Fig. 4. An operating frequency of 20 kHz is chosen for the switches as the latest SiC MOSFET can operate up to 48 kHz [32]. In Fig. 4, x (=AB, BC, and CA) denotes the phases of the power grid to which the rectifier is connected. For example, x = AB means that the rectifier is connected to the Phase-A and Phase-B lines. v_{gx} and $i_{\mathrm{MMC}x}$ represent the input voltage and current of the rectifier, respectively; $V_{\mathrm{dc}-x1}$ and $V_{\mathrm{dc}-x2}$ are the dc-link voltages of the two full-bridge modules; $i_{\mathrm{dco}-x1}$ and $i_{\mathrm{dco}-x2}$ denote the output

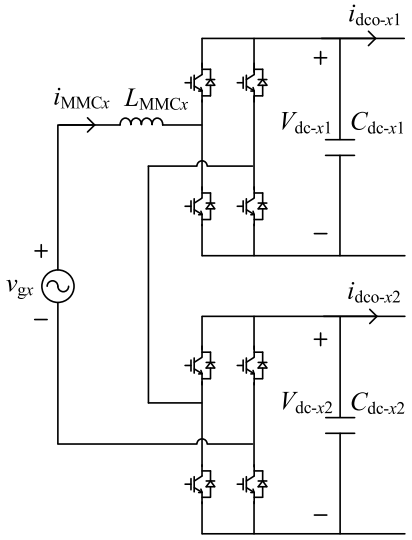

Fig. 4. Cascaded two H-bridge active rectifier of Phase x (x = AB, BC, and CA) in the MMC system.

TABLE II
SPECIFICATIONS OF THE CASCADED FULL-BRIDGE RECTIFIERS

$C_{dc\text{-}xi}$ (x = AB, BC, CA; i = 1, 2)	500 μF
$V_{dc\text{-}xi}$ (x = AB, BC, CA; i = 1, 2)	5.2 kV
L_{MMCx} (x = AB, BC, CA)	30 mH
V_{gx} (x = AB, BC, CA)	6.6 kV (50 Hz)
Switching Frequency	20 kHz

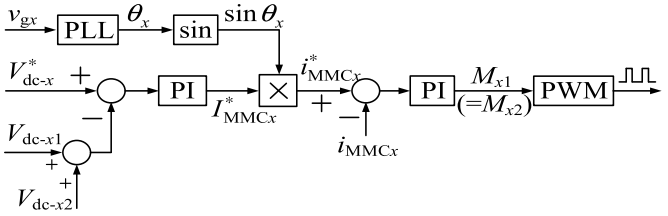

Fig. 5. Block diagram of the voltage and current control of the ac–dc active rectifier.

currents of the two modules. The rectifier parameters [33] are listed in Table II.

Fig. 5 shows the control block diagram for the cascaded full-bridge rectifier. First, the difference between the sum of the dc-link voltages (V_{dc-x1} and V_{dc-x2}) and its setpoint value $V^*_{dc\text{-}x}$ is processed by a proportional-integral (PI) controller to produce the magnitude reference I^*_{MMCx} of the MMC current, i.e.

$$I^*_{MMCx} = k_{p1}\left(V^*_{dc\text{-}x} - V_{dc\text{-}x1} - V_{dc\text{-}x2}\right) + k_{i1}\int \left(V^*_{dc\text{-}x} - V_{dc\text{-}x1} - V_{dc\text{-}x2}\right)dt. \quad (2)$$

Next, the phase information θ_x of the grid voltage v_{gx} is extracted with the phase-locked loop (PLL). By multiplying I^*_{MMCx} and $\sin\theta_x$, the reference i^*_{MMCx} of the MMC current is obtained. Then, the error between the MMC current i_{MMCx} and its reference i^*_{MMCx} is processed with a PI controller to obtain the modulation indices M_{x1} and M_{x2}, i.e.

$$M_{x1} = M_{x2} = k_{p2}\left(i^*_{MMCx} - i_{MMCx}\right) + k_{i2}\int \left(i^*_{MMCx} - i_{MMCx}\right)dt. \quad (3)$$

Finally, M_{x1} and M_{x2} will be modulated into pulses to control the switching patterns of the two full-bridge modules, respectively.

2) Second DC–AC–DC Power Conversion With a Stepped-Down Transformer: The dc–ac–dc stage is a typical DAB that utilizes two full bridges at both the primary and secondary sides. The output of each full-bridge module of the rectifier is connected to a DAB module, as shown in Fig. 6. Here, $i_{DABo-xi}$ denotes the output current of the secondary-side full bridge. v_{o-xi} and i_{o-xi} are the output voltage and current of the DAB module, respectively. The turns ratio of the transformer is N_1: N_2. The circuit structure of Fig. 6 supports reversible power flow and provides galvanic isolation. The parameters of the DAB module are listed in Table III.

For simplicity, the conventional single phase shift control method in [34] is adopted for the DAB. The duty cycles of the two full bridges are fixed at 0.5, and the pulses of the two full-bridges are phase shifted relative to one another. Fig. 7 illustrates the controller for the DAB output voltage, where D_{PS-xi} is the phase shift duty cycle. The controller first calculates the voltage error between the DAB output voltage V_{o-xi} and its setpoint value V^*_{o-xi}. Then, a PI controller generates the required phase shift duty cycle D_{PS-xi} for the DAB.

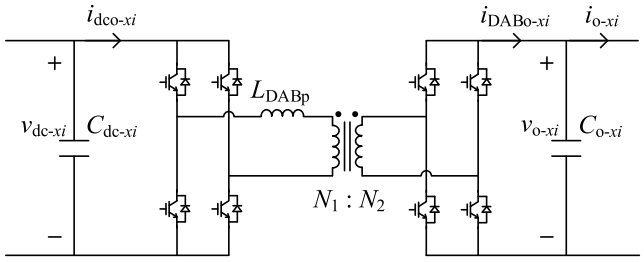

Fig. 6. ith (i = 1, 2) DAB module of Phase x (x = AB, BC, and CA) in the MMC system.

TABLE III
SPECIFICATIONS OF THE DAB MODULE

Rated power	25 kW
$V_{o\text{-}xi}$ (x = AB, BC, CA; i = 1, 2)	800 V
$C_{o\text{-}xi}$ (x = AB, BC, CA; i = 1, 2)	2000 μF
Turn's ratio of the transformer	7:1
L_{DABp} (including the leakage inductance of the transformer)	7 mH
Magnetizing inductance of the transformer	50 mH
Switching frequency	20 kHz

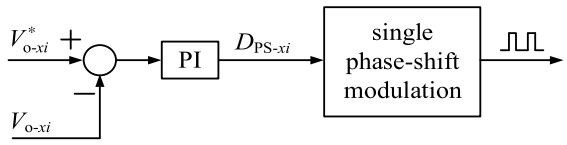

Fig. 7. Block diagram of the DAB voltage control.

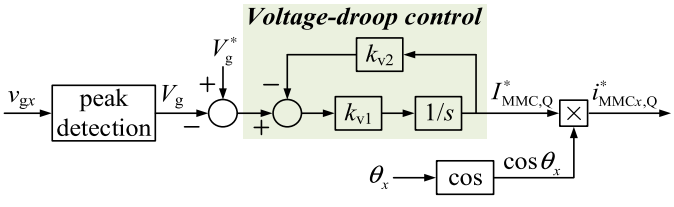

Fig. 8. Block diagram of the input voltage control of the MMC with ES functions.

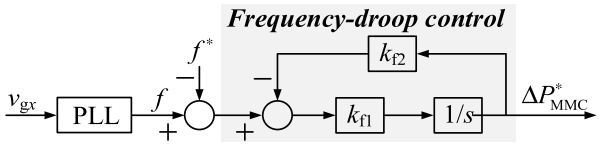

Fig. 9. Block diagram of the input frequency control of the MMC with ES functions.

B. Bidirectional AC–DC Power Converter System With Input Electric Spring Control

1) Input Voltage Control of ES-Based MMC for Regulating the Voltage of the Distribution Network: The block diagram of the input voltage control of the MMC with ES functions is shown in Fig. 8. The control of the input voltage is achieved by controlling the reactive power generation of the MMC.

First, the peak value V_g of the line-to-line input voltage v_{gx} is detected and compared with a preset reference V_g^* (e.g., $V_g^* = 6.6 \times \sqrt{2} = 9.334$ kV for a 6.6-kV distribution line). Then, the difference between V_g and V_g^* is processed by a voltage-droop controller to produce the magnitude reference $I^*_{\mathrm{MMC,Q}}$ of the MMC reactive current, i.e.

$$I^*_{\mathrm{MMC,Q}} = -\frac{1}{k_{v2}}\left(V_g - V_g^*\right). \tag{4}$$

In Fig. 8, an integration path is added in the voltage-droop controller to limit the bandwidth of the controller, thus enhancing the system stability. The time constant of the voltage-droop controller is determined by

$$\tau_v = \frac{1}{k_{v1}k_{v2}}. \tag{5}$$

On the other hand, the phase information θ_x of the power grid is extracted from v_{gx} with a PLL (see Fig. 5). By multiplying $I^*_{\mathrm{MMC,Q}}$ and $\cos\theta_x$, the reference $i^*_{\mathrm{MMC,Q}}$ of the MMC reactive current is obtained.

With the input voltage control, $i^*_{\mathrm{MMC}x,Q}$ in Fig. 8 should be added into the reference current $i^*_{\mathrm{MMC}x}$ for the MMC in Fig. 5.

2) Input Frequency Control of ES-Based MMC for Regulating the Frequency of the AC Power Grid: The input frequency control is achieved by adjusting the power consumption of the MMC, as illustrated in Fig. 9. The grid frequency f is first estimated from the input voltage v_{gx} with a PLL. Then, f is compared with a preset reference f^*, which should be the nominal frequency value of the power grid (e.g., 50 Hz in Singapore). A frequency-droop controller is designed to yield the power adjustment value $\Delta P^*_{\mathrm{MMC}}$ of the MMC from the error between f and f^*, i.e.

$$\Delta P^*_{\mathrm{MMC}} = \frac{1}{k_{f2}}(f - f^*). \tag{6}$$

When $f > f^*$, we have $\Delta P^*_{\mathrm{MMC}} > 0$, meaning to increase the power consumption of the MMC; when $f < f^*$, we have $\Delta P^*_{\mathrm{MMC}} < 0$, meaning to reduce the power consumption of the MMC. In particular, if the total power consumption of the MMC satisfies $P_{\mathrm{MMC}} + \Delta P^*_{\mathrm{MMC}} < 0$, then the MMC will operate in the reverse-power-flow mode.

Similar to the voltage-droop controller, an integration path is also added to the frequency-droop controller to enhance stability. The time constant of the frequency-droop controller is determined by

$$\tau_f = \frac{1}{k_{f1}k_{f2}}. \tag{7}$$

3) Average Model of the MMC: To facilitate the study of the behavior of the microgrid, the average model of the MMC, which neglects all switching details, is built below. As the MMC system in Fig. 2 consists of three parts (i.e., the rectifiers, the DABs, and the load), its average model can be obtained by deriving the average models of these three parts separately.

a) Average model of the active rectifiers: The rectifier of Phase x (x = AB, BC, and CA) in the MMC system, which is displayed in Fig. 4, can be described by the following state equations:

$$L_{\mathrm{MMC}}\frac{\mathrm{d}i_{\mathrm{MMC}x}}{\mathrm{d}t} = v_{3x} - M_{x1}v_{\mathrm{dc\text{-}}x1} - M_{x2}v_{\mathrm{dc\text{-}}x2} \tag{8}$$

$$C_{\mathrm{dc\text{-}}x1}\frac{\mathrm{d}v_{\mathrm{dc\text{-}}x1}}{\mathrm{d}t} = M_{x1}i_{\mathrm{MMC}x} - i_{\mathrm{dco\text{-}}x1} \tag{9}$$

$$C_{\mathrm{dc\text{-}}x2}\frac{\mathrm{d}v_{\mathrm{dc\text{-}}x2}}{\mathrm{d}t} = M_{x2}i_{\mathrm{MMC}x} - i_{\mathrm{dco\text{-}}x2}. \tag{10}$$

b) Average model of the DABs: Reference [34] gives the equation regarding the output current $i_{\mathrm{DABo}-xi}$ of the DAB module. Considering the reversible-power-flow requirement of the MMC system, the unidirectional equation of $i_{\mathrm{DABo}-xi}$ in [34] is extended into a bidirectional version, i.e.

$$i_{\mathrm{DABo\text{-}}xi} = \frac{N_1 v_{\mathrm{dc\text{-}}xi} D_{\mathrm{PS\text{-}}xi}(1 - |D_{\mathrm{PS\text{-}}xi}|)}{2N_2 f_s L_{\mathrm{DABp}}}. \tag{11}$$

A positive $D_{\mathrm{PS}-xi}$ corresponds to power flowing from the primary side to the secondary side, while a negative $D_{\mathrm{PS}-xi}$ indicates a reverse power flow.

The state equation of the output capacitor C_{o-xi} is given by

$$C_{o-xi}\frac{\mathrm{d}v_{o-xi}}{\mathrm{d}t} = i_{\mathrm{DABo\text{-}}xi} - i_{o-xi}. \tag{12}$$

According to the principle of conservation of energy, the DAB module is also governed by

$$v_{\mathrm{dc\text{-}}xi}i_{\mathrm{dco\text{-}}xi} = v_{o-xi}i_{\mathrm{DABo\text{-}}xi}. \tag{13}$$

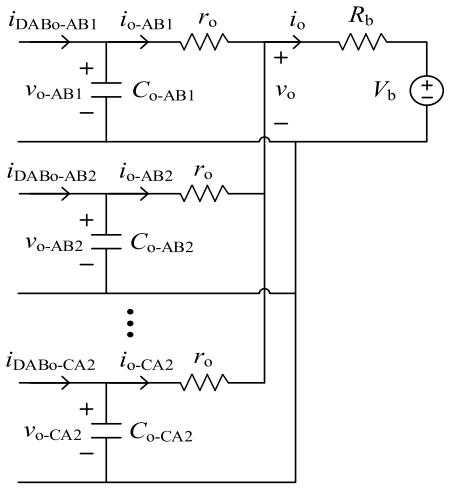

Fig. 10. Load part in the bidirectional ac–dc MMC system.

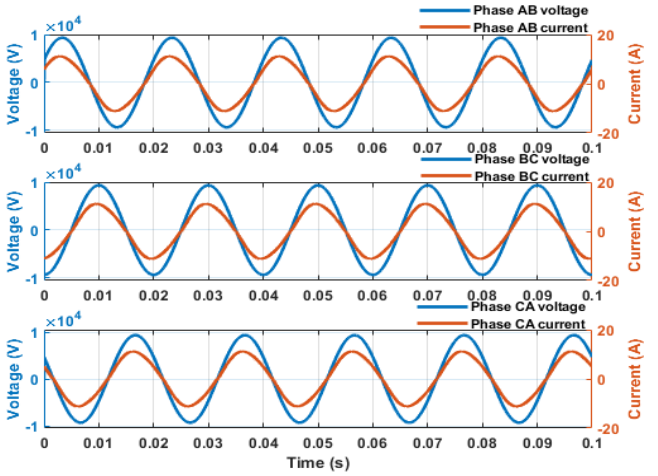

Fig. 11. Waveforms of the three-phase input voltages and currents of the MMC at rated output power.

c) Average model of the load: Fig. 10 gives the circuit of the load part. Here, a small wire resistance r_o is considered, so that the six voltages $v_{o-\mathrm{AB1}}$, $v_{o-\mathrm{AB2}}, \ldots, v_{o-\mathrm{CA2}}$ can be connected in parallel. The battery load is modeled as an adjustable voltage source V_b in series with a resistor R_b. The value of V_b determines the charging/discharging power of the battery.

According to Kirchhoff's current and voltage laws, one has

$$v_o = v_{o-xi} - r_o i_{o-xi} \tag{14}$$

$$v_o = V_b + R_b i_o \tag{15}$$

$$i_o = \sum_{x,i} i_{o-xi}. \tag{16}$$

In summary, the set of equations from (8) to (16) forms the average model of the MMC system, which can be combined with the control laws given in Figs. 5 and 7–9 to describe the closed-loop performance of the bidirectional ac–dc power converter system.

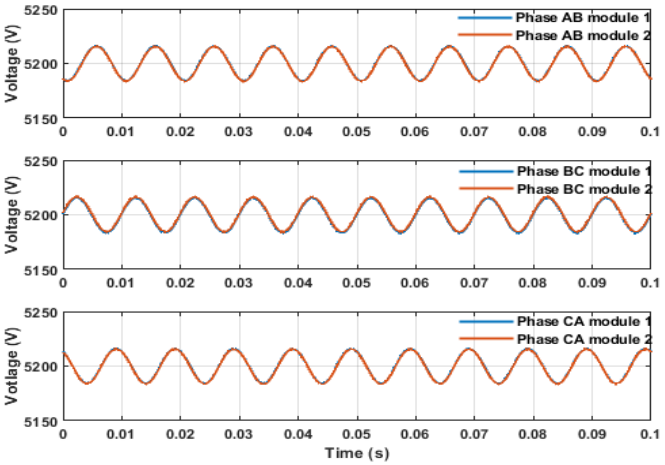

Fig. 12. Waveforms of the dc-link voltages of the rectifiers at rated output power.

IV. Bidirectional Power Converter Operations and Its Interactions With an AC Microgrid

A. Bidirectional AC–DC Power Converter Operations

The steady-state performance, transient performance, and bidirectional-power-flow operation of the MMC system are examined with power circuit simulation based on the PSIM software package. The high-frequency switching operation of the full converter system is included in the simulation.

1) Steady-State Performance of Input Power Factor and Output DC Voltage Control of the ES-Based MMC: The power flow from the ac grid to the dc grid is first considered. In this converter test, the MMC draws a rated power of 150 kW from a stiff 6.6-kV grid to the 800-V dc power grid with a resistive load. The input current and power factor, the intermediate dc voltage link, the voltage and current of the DAB with the medium-frequency isolation transformer, and the output dc grid voltage are examined. The simulation waveforms of the power converter system are shown in Figs. 11–13. Fig. 11 shows the three-phase input voltages and currents of the MMC at rated power. The power factor is 0.998, and the total demand distortion (TDD) of the currents is 4.34%, which complies with the IEEE 519 standard of harmonic regulation.

The dc-link voltages of the three-phase rectifiers are shown in Fig. 12. The peak-to-peak voltage ripples are less than 0.5% for all six full-bridge modules, which indicate good regulation of the dc-link voltages at the rated output power. Fig. 13 displays the primary-side and secondary-side voltages and currents of a single DAB module. An obvious phase delay of the secondary-side voltage with respect to the primary-side voltage can be observed, enabling power delivery from the primary side to the secondary side.

2) Transient Performance of Input Power Factor and Output DC Voltage Control of the ES-Based MMC: In the second converter test, the output power of the ac–dc power converter is changed from 150 to 75 kW at $t = 0.15$ s. The simulation waveforms are shown in Figs. 14 and 15. Fig. 14 shows the three-phase input voltages and currents of the MMC. Note that unity power factor is maintained in both the full-load and

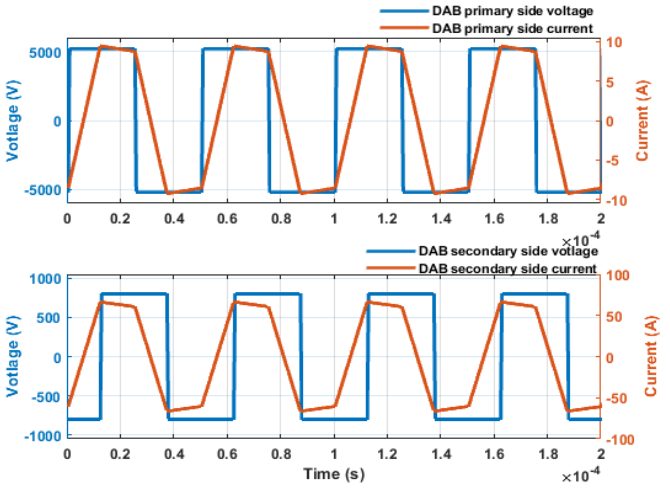

Fig. 13. Waveforms of the primary-side and secondary-side voltages and currents of a single DAB module at rated output power.

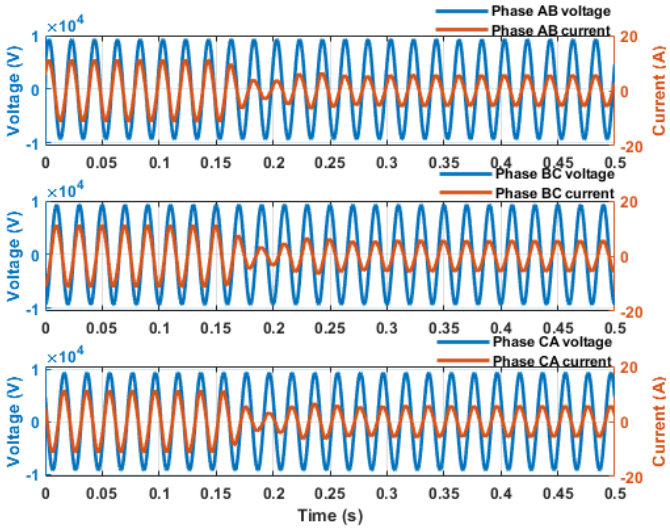

Fig. 14. Waveforms of the three-phase input voltages and currents of the MMC when the power changes from full load to half load at $t = 0.15$ s.

half-load conditions. The dc-link voltages of the three-phase rectifiers are displayed in Fig. 15. These voltages are well maintained within 5200 ± 50 V during the transient operation. Figs. 14 and 15 indicate that the rectifiers reach the steady state at around 0.2 s.

Fig. 16 illustrates the output voltage and current of the ac–dc power converter system. It can be observed that a spike appears in the output voltage at the transient instant. Nonetheless, the voltage spike is less than 5% of the nominal value and the output voltage returns to 800 V in 0.1 s. The result verifies that the output voltage of the ac–dc power converter system is well regulated.

3) Bidirectional-Power-Flow Operation of the ES-Based MMC With Both Input Power Factor and Output DC Voltage Control: In this converter test, the ac–dc power converter system initially draws 75-kW power from the ac grid to charge the dc battery load. At $t = 0.15$ s, the direction of the power flow is reversed, and the ac–dc power converter system feeds

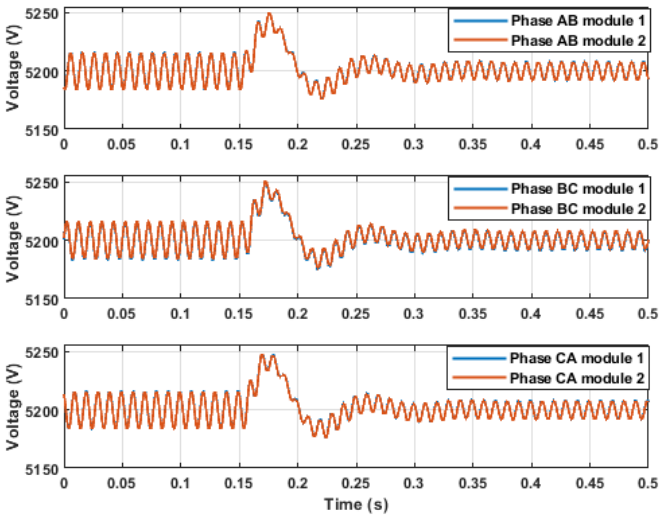

Fig. 15. Waveforms of the dc-link voltages of the rectifiers when the power changes from full load to half load at $t = 0.15$ s.

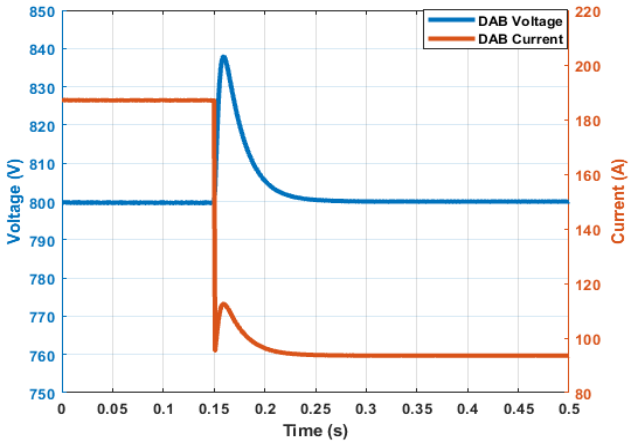

Fig. 16. Waveforms of the output voltage and current of the MMC when the power changes from full load to half load at $t = 0.15$ s.

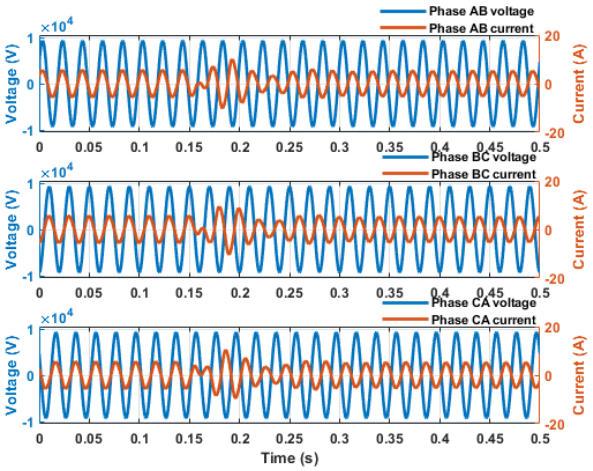

Fig. 17. Waveforms of the three-phase input voltages and currents of the MMC in the reversible-power-flow test.

the power of 75 kW back into the ac grid by discharging the battery. The simulation waveforms are shown in Figs. 17–19.

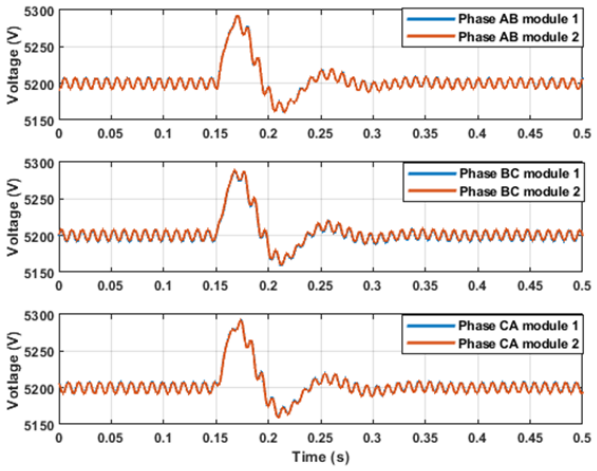

Fig. 18. Waveforms of the dc-link voltages of the rectifiers in the reversible-power-flow test.

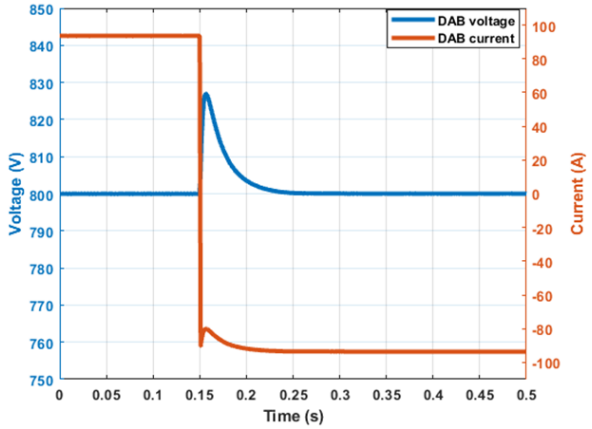

Fig. 19. Waveforms of the output voltage and current of the MMC in the reversible-power-flow test.

Fig. 17 shows the three-phase input voltages and currents of the MMC. The voltage and current of each phase are initially in phase, respectively. After $t = 0.16$ s, they become out of phase, indicating the reverse change of the power flow direction. The power factor keeps unity throughout the whole process. Fig. 18 shows the output voltage and current of the ac–dc power converter system. They are kept within $\pm 2\%$ of the nominal value and reach the steady state in about 0.3 s. Fig. 19 shows the output voltage and current of the ac–dc power converter system. The output current changes from $+93$ to -93 A at $t = 0.15$ s, confirming the change of the battery operating mode from charging to discharging. A voltage spike of 26 V can be observed in the output voltage. Nonetheless, the output voltage is controlled back to its nominal value after 0.1 s. These results verify the effectiveness of the proposed converter system structure and the controller design.

B. AC-Microgrid to DC-Power Grid System Interactions Through the ES-Based MMC

Fig. 20 shows a 6.6-kV three-bus ac microgrid for illustration of the ES functions of the MMC. The microgrid consists of a generator G on Bus 1, a WT and a resistive load on

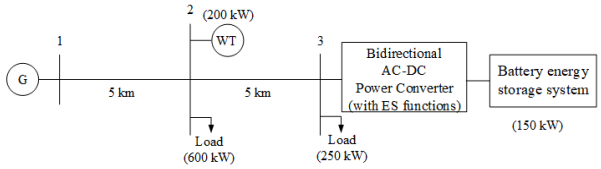

Fig. 20. 6.6-kV three-bus ac microgrid linked with the 800-V dc grid via the bidirectional ac–dc power MMC converter with ES functions.

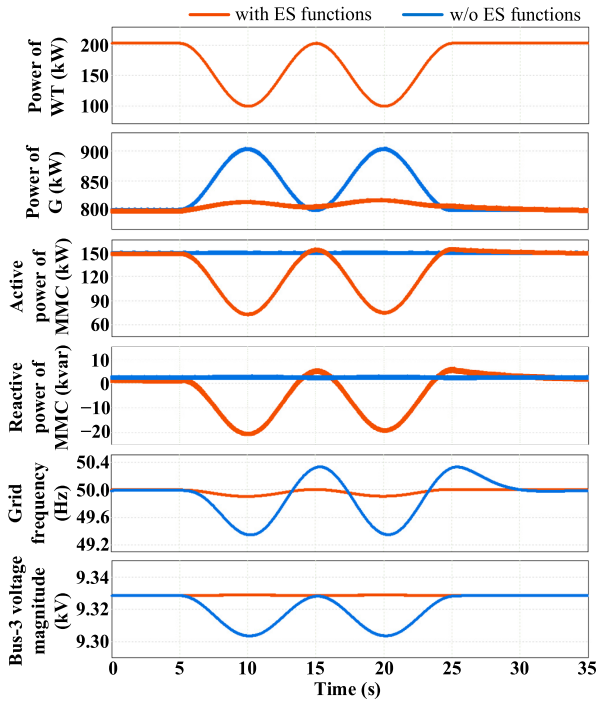

Fig. 21. Simulation waveforms of Scenario 1 using ES-based ac–dc MMC to stabilize the power grid with fluctuating renewable power.

Bus 2, and an MMC-fed battery load and a resistive load on Bus 3. There are two 5-km distribution lines between Bus 1 and Bus 2 and between Bus 2 and Bus 3, respectively. The wire resistance and inductance of the distribution line are 0.237 Ω/km and 1.064 mH/km, respectively, with reference to [35]. The initial power of each element is also marked in Fig. 20. Two scenarios are considered in the simulation study below.

1) Scenario 1: Microgrid Stabilization by ES Against Power Fluctuations of Renewable Power: In the first system test, the output power of the WT begins to fluctuate between 100 and 200 kW in a sinusoidal fashion from $t = 5$ s. This power fluctuation has a period of 10 s and lasts for 20 s. The simulation waveforms without and with ES functions are compared in Fig. 21.

The power fluctuation of the WT (the first plot of Fig. 21) causes the power generator to alter its output. Without ES functions, the output power of the generator swings significantly (blue trace in the second plot) when the load consumption remains constant (blue trace in the third plot). As a result, the grid frequency swings from 49.4 to 50.3 Hz (blue trace in the fifth plot). Moreover, the bus voltages in the microgrid are also disturbed by the fluctuating wind power (blue trace in the

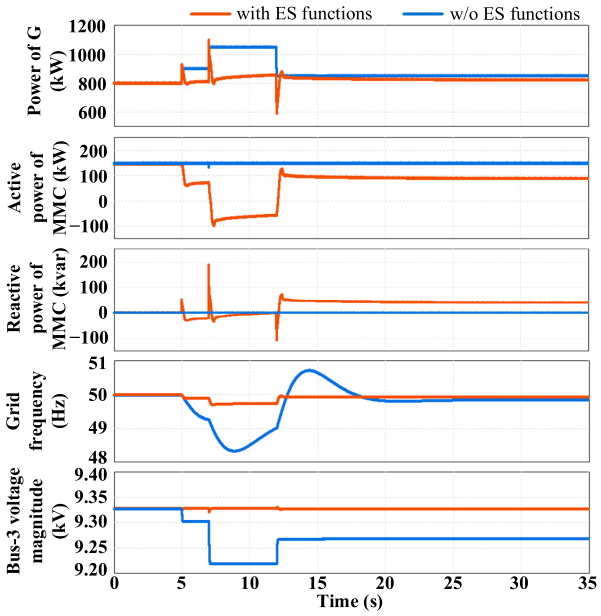

Fig. 22. Simulation waveforms of Scenario 2 using ES-based MMC to stabilize power grid with both fluctuating renewable power and sudden load change.

sixth plot). The reactive power of the MMC remains constant (blue trace in the fourth plot) because there is no ES function.

With ES functions activated, the power consumption of the MMC-fed load is adaptive to the wind power fluctuation (orange trace in the third plot) to dynamically compensate the power change in the microgrid. This fast DSM significantly mitigates the power fluctuation of the generator (orange trace in the second plot) and stabilizes the voltage and frequency of the microgrid (orange traces in the sixth and fifth plots). The ES functions are illustrated in the active and reactive power compensations provided on the ac side of the MMC (orange traces in the third and fourth plots) to regulate the ac grid frequency and voltage, respectively. As a result, the variation range of the grid frequency is reduced to 49.9–50.0 Hz, and the fluctuation of the Bus-3 voltage magnitude is largely mitigated to 1 V. The results in Fig. 21 verify that the ES control of the MMC can effectively regulate its input voltage and the grid frequency.

2) Scenario 2: Grid Stabilization by ES Against Power Fluctuations of Renewable Power and Sudden Load Change: To evaluate the ES functions, the second power system test involves both power fluctuations of renewables and large load change. The wind power drops from 200 to 100 kW at $t = 5$ s and then rises to 300 kW at $t = 12$ s. The resistive load on Bus 3 also increases from 250 to 400 kW at $t = 7$ s. Fig. 22 presents the simulation waveforms.

Without ES functions, the battery load consumes constant power (blue trace in the second plot of Fig. 22). When the wind power drops at $t = 5$ s, the generator power has to increase (blue trace in the first plot) to feed the constant battery load, but the governor control fails to regulate the grid frequency within a tight tolerance. As shown in the blue trace in the fourth plot in Fig. 22, the grid frequency temporarily drops to about 49.2 Hz from 5 to 7 s. When the load demand increases at 7 s, the grid frequency drops further to 48.3 Hz. When the wind power rises to 300 kW at 12 s, the grid frequency rises to 50.7 Hz. Such a large frequency deviation can exceed the acceptable range in some countries (e.g., 49.5–50.5 Hz in the U.K. [36]). In addition, there is a voltage drop of 110 V (1.2%) on Bus 3 (blue trace in the fifth plot), which is undesirable.

With ES functions activated, the battery load consumes power adaptively as shown in the orange trace of the second plot. This fast DSM absorbs most of the power fluctuation of the WT and reduces the power variation of the generator, as shown in the orange trace of the first plot. Consequently, the frequency variation range is significantly narrowed down to 49.7–50.0 Hz (orange trace in the fourth plot), and the Bus-3 voltage magnitude is successfully maintained around its nominal level (orange trace in the fifth plot). The ES actions are illustrated in the active and reactive powers in the second and third plots in Fig. 22, respectively. The active power of the bidirectional ac–dc MMC drops below zero between $t = 7$ s and $t = 12$ s, indicating that the MMC temporarily reverses its power flow direction and operates as a power source to support the frequency stability of the ac microgrid. The reactive power provided by the ES-based MMC is successful in maintaining the voltage stability. The effectiveness of the MMC with ES functions in voltage and frequency control in the microgrid is once again verified.

V. Conclusion

The urgent need for large-scale EV charging infrastructure in big cities such as Singapore imposes new challenges in increasing electric power supply capability in existing multistorey carparks built before the EV era. The need for large-scale intermittent renewable energy generation also leads to power fluctuation and potential power system stability problems. This study proposes the combined uses of EV charging infrastructure with ES functions and renewable energy as a complementary solution to combat climate change. The novelty of this article involves a bidirectional ac–dc power converter system with ES functions installed on the ac side at the distribution voltage level. It can generate a dc voltage link for a dc power grid directly from the distribution network of an ac power grid. The concept is demonstrated with the use of an MMC with DAB modules. Because of the modular nature, the power capability of the proposed ac–dc power converter system is expandable based on the parking capacity of the multistorey carparks. It is a feasible solution to provide the dc power grid for large-scale EV charging infrastructure in multistorey carparks in order to accelerate the adoption of EVs. With the bidirectional power flow capability and ES functions (i.e., active and reactive power compensation control on the ac side of the ac–dc power converter system), the proposed solution can mitigate frequency and voltage fluctuation of the ac power grid, and therefore, it enables power companies to adopt more renewable energy generation. The proposal has been evaluated in both converter tests and ac microgrid tests through comprehensive simulations. The results confirm the feasibility and validity of the proposal in a small microgrid. The bidirectional MMC for large battery load, such as large EV-charging infrastructure, will form the

core element for future large-scale power system stability studies.

APPENDIX

For the transformer in the DAB module, the inductance L_{DABp} is most significant as it has a large impact on the output current $i_{\mathrm{DABo}-xi}$ of the DAB according to (11) in this article, which is rewritten as follows:

$$i_{\mathrm{DABo\text{-}}xi} = \frac{N_1 v_{\mathrm{dc\text{-}}xi} D_{\mathrm{PS\text{-}}xi}(1 - |D_{\mathrm{PS\text{-}}xi}|)}{2N_2 f_s L_{\mathrm{DABp}}}. \tag{17}$$

Large values of L_{DABp} will reduce the DAB's output current and thus limit the maximum transferrable power, while too small values of L_{DABp} will make the DAB's output current sensitive to disturbances of the input voltage $v_{\mathrm{dc}-xi}$ and the phase shift $D_{\mathrm{PS}-xi}$, and thereby resulting in noisy current and even system instability.

In this study, the nominal values of the DAB module are as follows: $I^n_{\mathrm{DABo\text{-}}xi} = 31.25$ A, $V^n_{\mathrm{dc\text{-}}xi} = 5.2$ kV, $f_s = 20$ kHz, and $N_1/N_2 = 7$. The range of $D_{\mathrm{PS}-xi}$ is between -0.5 and 0.5. To meet our power requirement, it should be satisfied that

$$\max(i_{\mathrm{DABo\text{-}}xi}) \geq I^n_{\mathrm{DABo\text{-}}xi}. \tag{18}$$

Substituting (17) into (18) gives

$$L_{\mathrm{DABp}} \leq 7.28 \text{ mH}. \tag{19}$$

Therefore, we set L_{DABp} to be 7 mH in our design. This inductance can be achieved either with the leakage inductance of the transformer alone [37] or with the help of an external inductor [33]. In our DAB module, we employ an external inductor and L_{DABp} includes both the inductance of the external inductor and the leakage inductance of the transformer. For DABs, the magnetizing inductance of the transformer is typically much larger than the inductance L_{DABp} [32], [38], [39]. Therefore, we follow this common practice in this study.

REFERENCES

[1] *Paris Agreement*. Assessed: Oct. 14, 2021. [Online]. Available: https://unfccc.int/sites/default/files/english_paris_agreement.pdf

[2] *Singapore Green Plan 2030*. Assessed: Oct. 14, 2021. [Online]. Available: https://www.greenplan.gov.sg/

[3] (1992). *Shining on National Renewable Energy Laboratory*. Technical Report NREL/TP-463-4856. Accessed: Oct. 14, 2021. [Online]. Available: http://rredc.nrel.gov/solar/pubs/shining/chap4.html

[4] P. Kundur, "Introduction to power system stability problem," in *Power System Stability and Control*. New York, NY, USA: McGraw-Hill, 1994, pp. 17–41.

[5] D. Westermann and A. John, "Demand matching wind power generation with wide-area measurement and demand-side management," *IEEE Trans. Energy Convers.*, vol. 22, no. 1, pp. 145–149, Mar. 2007.

[6] P. Palensky and D. Dietrich, "Demand side management: Demand response, intelligent energy systems, and smart loads," *IEEE Trans. Ind. Informat.*, vol. 7, no. 3, pp. 381–388, Aug. 2011.

[7] P. T. Krein and J. A. Galtieri, "Active management of photovoltaic system variability with power electronics," *IEEE J. Emerg. Sel. Topics Power Electron.*, vol. 9, no. 6, pp. 6507–6523, Dec. 2021.

[8] (Jun. 2016). WindEurope. *WindEurope Views on Curtailment of Wind Power and its Links to Priority and Dispatch*. [Online]. Available: https://windeurope.org/wp-content/uploads/files/policy/position-papers/WindEurope-Priority-Dispatch-and-Curtailment.pdf

[9] A.-H. Mohsenian-Rad, V. W. S. Wong, J. Jatskevich, R. Schober, and A. Leon-Garcia, "Autonomous demand-side management based on game-theoretic energy consumption scheduling for the future smart grid," *IEEE Trans. Smart Grid*, vol. 1, no. 3, pp. 320–331, Dec. 2010.

[10] M. Parvania and M. Fotuhi-Firuzabad, "Demand response scheduling by stochastic SCUC," *IEEE Trans. Smart Grid*, vol. 1, no. 1, pp. 89–98, Jun. 2010.

[11] A. J. Conejo, J. M. Morales, and L. Baringo, "Real-time demand response model," *IEEE Trans. Smart Grid*, vol. 1, no. 3, pp. 236–242, Dec. 2010.

[12] A.-H. Mohsenian-Rad and A. Leon-Garcia, "Optimal residential load control with price prediction in real-time electricity pricing environments," *IEEE Trans. Smart Grid*, vol. 1, no. 2, pp. 120–133, Sep. 2010.

[13] S. C. Lee, S. J. Kim, and S. H. Kim, "Demand side management with air conditioner loads based on the queuing system model," *IEEE Trans. Power Syst.*, vol. 26, no. 2, pp. 661–668, May 2011.

[14] A. Brooks, E. Lu, D. Reicher, C. Spirakis, and B. Weihl, "Demand dispatch," *IEEE Power Energy Mag.*, vol. 8, no. 3, pp. 20–29, May/Jun. 2010.

[15] S. Y. Hui, C. K. Lee, and F. F. Wu, "Electric springs—A new smart grid technology," *IEEE Trans. Smart Grid*, vol. 3, no. 3, pp. 1552–1561, Sep. 2012.

[16] C.-K. Lee, H. Liu, S.-C. Tan, B. Chaudhuri, and S.-Y.-R. Hui, "Electric spring and smart load: Technology, system-level impact, and opportunities," *IEEE J. Emerg. Sel. Topics Power Electron.*, vol. 9, no. 6, pp. 6524–6544, Dec. 2021.

[17] P. Tsao, M. Senesky, and S. R. Sanders, "An integrated flywheel energy storage system with homopolar inductor motor/generator and high-frequency drive," *IEEE Trans. Ind. Appl.*, vol. 39, no. 6, pp. 1710–1725, Nov./Dec. 2003.

[18] S. Rahman, I. A. Khan, and M. H. Amini, "A review on impact analysis of electric vehicle charging on power distribution systems," in *Proc. 2nd Int. Conf. Smart Power Internet Energy Syst. (SPIES)*, Sep. 2020, pp. 420–425.

[19] D. Strickland *et al.*, "Feasibility study: Investigation of car park-based V2G services in the U.K. central hub," *J. Eng.*, vol. 2019, no. 17, pp. 3967–3971, Jun. 2019.

[20] L. Rubino, G. Rubino, and P. Marino, "High step down multilevel resonant buck converter with high voltage ratio," in *Proc. Int. Symp. Power Electron., Electr. Drives, Autom. Motion (SPEEDAM)*, Capri, Italy, Jun. 2016, pp. 22–24.

[21] X. Zhang and T. C. Green, "The modular multilevel converter for high step-up ratio DC–DC conversion," *IEEE Trans. Ind. Electron.*, vol. 62, no. 8, pp. 4925–4936, Aug. 2015.

[22] S. Cui, N. Soltau, and R. W. De Doncker, "A high step-up ratio soft-switching DC–DC converter for interconnection of MVDC and HVDC grids," *IEEE Trans. Power Electron.*, vol. 33, no. 4, pp. 2986–3001, Apr. 2018.

[23] D. Xing *et al.*, "MMC-based high gain solid-state transformers for energy storage applications," in *Proc. IEEE Appl. Power Electron. Conf. Expo. (APEC)*, Jun. 2021, pp. 1996–2002.

[24] S. Y. R. Hui, S. C. Tan, and C. Mi, "Bidirectional AC-DC power conversion method and apparatus," U.S. Patent 63 202 774, Jun. 23, 2021.

[25] A. Lesnicar and R. Marquardt, "An innovative modular multilevel converter topology suitable for a wide power range," in *Proc. IEEE Bologna Power Tech Conf.*, Bologna, Italy, Jun. 2003, p. 6.

[26] M. A. Perez, S. Bernet, J. Rodriguez, S. Kouro, and R. Lizana, "Circuit topologies, modeling, control schemes, and applications of modular multilevel converters," *IEEE Trans. Power Electron.*, vol. 30, no. 1, pp. 4–17, Jan. 2015.

[27] S. Dehnath, J. Qin, B. Bahrani, M. Saeedifard, and P. Barbosa, "Operation, control and applications of the modular multilevel converters: A review," *IEEE Trans. Power Electron.*, vol. 30, no. 1, pp. 37–53, Jan. 2015.

[28] R. W. A. A. De Doncker, D. M. Divan, and M. H. Kheraluwala, "A three-phase soft-switched high-power-density DC/DC converter for high-power applications," *IEEE Trans. Ind. Appl.*, vol. 27, no. 1, pp. 63–73, Jan./Feb. 1991.

[29] J.-S. Lai and F. Zheng Peng, "Multilevel converters—A new breed of power converters," *IEEE Trans. Ind. Appl.*, vol. 32, no. 3, pp. 509–517, Jun. 1996.

[30] J. E. Huber, J. Böhler, D. Rothmund, and J. W. Kolar, "Analysis and cell-level experimental verification of a 25 kW all-SiC isolated front end 6.6 kV/400 V AC-DC solid-state transformer," *CPSS Trans. Power Electron. Appl.*, vol. 2, no. 2, pp. 140–148, Aug. 2017.

[31] M. R. Islam, Y. Guo, and J. Zhu, *Power Converters for Medium Voltage Networks*. New York, NY, USA: Springer, 2014.

[32] D. Rothmund, T. Guillod, D. Bortis, and J. W. Kolar, "99% efficient 10 kV SiC-based 7 kV/400 V DC transformer for future data centers," *IEEE J. Emerg. Sel. Topics Power Electron.*, vol. 7, no. 2, pp. 753–767, Jun. 2019.

[33] J. Shi *et al.*, "Research on voltage and power balance control for cascaded modular solid-state transformer," *IEEE Trans. Power Electron.*, vol. 26, no. 4, pp. 1154–1166, Apr. 2011.
[34] C. Mi, H. Bai, C. Wang, and S. Gargies, "Operation, design and control of dual H-bridge-based isolated bidirectional DC–DC converter," *IET Power Electron.*, vol. 1, no. 4, pp. 507–517, 2008.
[35] A. Kaneko, Y. Hayashi, T. Anegawa, H. Hokazono, and Y. Kuwashita, "Evaluation of an optimal radial-loop configuration for a distribution network with PV systems to minimize power loss," *IEEE Access*, vol. 8, pp. 220408–220421, 2020.
[36] *The Grid Code*, Nat. Grid ESO, Warwick, U.K., 2021.
[37] H. Qin and J. W. Kimball, "Generalized average modeling of dual active bridge DC–DC converter," *IEEE Trans. Power Electron.*, vol. 27, no. 4, pp. 2078–2084, Apr. 2012.
[38] J. Saha, A. Subramanium, and S. K. Panda, "Design of integrated medium frequency transformer (iMFT) for dual-active-bridge (DAB) based solid-state-transformers," in *Proc. IEEE 12th Energy Convers. Congr. Expo. (ECCE-Asia)*, May 2021, pp. 893–898.
[39] Z. Qin, Z. Shen, F. Blaabjerg, and P. Bauer, "Transformer current ringing in dual active bridge converters," *IEEE Trans. Ind. Electron.*, vol. 68, no. 12, pp. 12130–12140, Dec. 2021.

Hin Sang Lam (Graduate Student Member, IEEE) received the B.Eng. degree (Hons.) in electrical engineering and the M.Phil. degree from The University of Hong Kong, Hong Kong, in 2018 and 2020, respectively. He is currently pursuing the Ph.D. degree with the School of Electrical and Electronic Engineering, Nanyang Technological University, Singapore.

His current research interests include power electronics, smart grids, and renewable energy conversion.

Huawei Yuan (Member, IEEE) received the B.Eng. and M.S. degrees in electrical engineering from Tsinghua University, Beijing, China, in 2013 and 2016, respectively, and the Ph.D. degree in electrical and electronic engineering from The University of Hong Kong, Hong Kong, in 2020.

He is currently a Research Fellow with the School of Electrical and Electronic Engineering, Nanyang Technological University, Singapore. His current research interests include the control of power electronic systems and the smart grid.

Siew-Chong Tan (Senior Member, IEEE) received the B.Eng. (Hons.) and M.Eng. degrees in electrical and computer engineering from the National University of Singapore, Singapore, in 2000 and 2002, respectively, and the Ph.D. degree in electronic and information engineering from The Hong Kong Polytechnic University, Hong Kong, in 2005.

He is currently a Professor with the Department of Electrical and Electronic Engineering, The University of Hong Kong, Hong Kong. His current research interests include power electronics and control, LED lightings, smart grids, and clean energy technologies.

Chunting Chris Mi (Fellow, IEEE) received the B.S.E.E. and M.S.E.E. degrees in electrical engineering from Northwestern Polytechnical University, Xi'an, China, in 1985 and 1988, respectively, and the Ph.D. degree in electrical engineering from the University of Toronto, Toronto, ON, Canada, in 2001.

He was with the University of Michigan, Dearborn, MI, USA, from 2001 to 2015. He is currently a Distinguished Professor and the Chair of the Department of Electrical and Computer Engineering and the Director of the Department of Energy (DOE)-funded Graduate Automotive Technology Education (GATE) Center for Electric Drive Transportation, San Diego State University, San Diego, CA, USA. His current research interests include electric drives, power electronics, electric machines, electrical and hybrid vehicles, wireless power transfer, and power electronics.

Dr. Mi is a Fellow of SAE. He was a recipient of the IEEE PELS Emerging Technology Award in 2019, IEEE Transaction on Power Electronics Best Paper Award, two IEEE Transaction on Power Electronics Prize Letter Awards, and the Albert W. Johnson Lecture Award, which is the highest distinction for any SDSU faculty.

Josep Pou (Fellow, IEEE) received the B.S., M.S., and Ph.D. degrees in electrical engineering from the Technical University of Catalonia (UPC)-Barcelona Tech, Barcelona, Spain, in 1989, 1996, and 2002, respectively.

From February 2013 to August 2016, he was a Professor with the University of New South Wales (UNSW), Sydney, NSW, Australia. From February 2001 to January 2002, and February 2005 to January 2006, he was a Researcher with the Center for Power Electronics Systems, Virginia Tech, Blacksburg, VA, USA. From January 2012 to January 2013, he was a Visiting Professor with the Australian Energy Research Institute, UNSW, Sydney. He is currently a Professor with Nanyang Technological University (NTU), Singapore, where he is the Cluster Director of power electronics with the Energy Research Institute, NTU (ERI@N) and a Co-Director of the Rolls-Royce, NTU Corporate Laboratory. He has authored more than 400 published technical papers and has been involved in several industrial projects and educational programs in the fields of power electronics and systems. His current research interests include modulation and control of power converters, multilevel converters, renewable energy, energy storage, power quality, high-voltage direct current (HVdc) transmission systems, and more-electrical aircraft and vessels.

Dr. Pou received the 2018 IEEE Bimal Bose Award for Industrial Electronics Applications in Energy Systems. He is an Associate Editor of the IEEE JOURNAL OF EMERGING AND SELECTED TOPICS IN POWER ELECTRONICS. He was a coeditor-in-chief and an Associate Editor of the IEEE TRANSACTIONS ON INDUSTRIAL ELECTRONICS.

S. Y. R. Hui (Fellow, IEEE) received the B.Sc. (Eng) degree (Hons.) in electrical and electronic engineering from the University of Birmingham, Birmingham, U.K., in 1984, and the D.I.C. and Ph.D. degrees in electrical engineering from the Imperial College London, London, U.K., in 1987.

He is currently the MediaTek Endowed Professor with Nanyang Technological University, Singapore, and a Chair Professor of power electronics with the Imperial College London. He has authored or coauthored over 300 journal papers. Over 120 of his patents have been adopted by industry worldwide. His current research interests include power electronics, wireless power, sustainable lighting, and smart grid. His inventions on wireless charging platform technology underpin key dimensions of Qi, the world's first wireless power standard, with freedom of positioning and localized charging features for wireless charging of consumer electronics. He also developed the Photo-Electro-Thermal Theory for LED Systems

He received the IEEE Rudolf Chope Research and Development Award and the IET Achievement Medal (The Crompton Medal) in 2010 and IEEE William E. Newell Power Electronics Award in 2015. He is a Fellow of the Australian Academy of Technological Sciences and Engineering, U.S. National Academy of Inventors, and Royal Academy of Engineering, U.K.